Computers in Biology and Medicine 142 (2022) 105174

Contents lists available at ScienceDirect

Computers in Biology and Medicine

journal homepage: www.elsevier.com/locate/compbiomed

Reconstruction of cardiac position using body surface potentials

Jake A. Bergquist [a,b,c,*], Jaume Coll-Font [d], Brian Zenger [a,b,c,e], Lindsay C. Rupp [a,b,c], Wilson W. Good [f], Dana H. Brooks [g], Rob S. MacLeod [a,b,c]

[a] Scientific Computing and Imaging Institute, University of Utah, 72 Central Campus Dr, Salt Lake City, UT, 84112, United States
[b] Nora Eccles Cardiovascular Research and Training Institute, University of Utah, 72 Central Campus Dr, Salt Lake City, UT, 84112, United States
[c] Department of Biomedical Engineering, University of Utah, 72 Central Campus Dr, Salt Lake City, UT, 84112, United States
[d] Cardiovascular Bioengineering Imaging (CBM) Lab at the Massachusetts General Hospital, Boston, MA, United States
[e] School of Medicine, University of Utah, 72 Central Campus Dr, Salt Lake City, UT, 84112, United States
[f] Acutus Medical, Carlsbad, CA, United States
[g] Department of Electrical and Computer Engineering, Northeastern University, Boston, MA, United States

ARTICLE INFO

Keywords:
Electrocardiographic imaging
Body surface potential mapping
Inverse problem
Optimization

ABSTRACT

Electrocardiographic imaging (ECGI) is a noninvasive technique to assess the bioelectric activity of the heart which has been applied to aid in clinical diagnosis and management of cardiac dysfunction. ECGI is built on mathematical models that take into account several patient specific factors including the position of the heart within the torso. Errors in the localization of the heart within the torso, as might arise due to natural changes in heart position from respiration or changes in body position, contribute to errors in ECGI reconstructions of the cardiac activity, thereby reducing the clinical utility of ECGI. In this study we present a novel method for the reconstruction of cardiac geometry utilizing noninvasively acquired body surface potential measurements. Our geometric correction method simultaneously estimates the cardiac position over a series of heartbeats by leveraging an iterative approach which alternates between estimating the cardiac bioelectric source across all heartbeats and then estimating cardiac positions for each heartbeat. We demonstrate that our geometric correction method is able to reduce geometric error and improve ECGI accuracy in a wide range of testing scenarios. We examine the performance of our geometric correction method using different activation sequences, ranges of cardiac motion, and body surface electrode configurations. We find that after geometric correction resulting ECGI solution accuracy is improved and variability of the ECGI solutions between heartbeats is substantially reduced.

1. Introduction

Electrocardiographic imaging (ECGI) is a computational methodology to noninvasively reconstruct the electrical activity of the heart using body surface electrocardiograms (ECGs) and a model of the torso volume conductor [1]. ECGI has been applied clinically and experimentally to a range of pathologies and applications including localizing sites of premature activation, localizing arrhythmogenic circuits, preoperative planning, and guiding ablation procedures [2–5]. Contemporary research and development of ECGI have produced a range of technical and experimental advances designed to address novel diseases and to improve accuracy, stability, and utility [1,6–8]. However, one source of error that reduces ECGI accuracy, and therefore clinical utility, that is generally not addressed outside of a limited set of studies, is error in the modeling of heart position within the chest [9–13].

The technical steps involved in most implementations of ECGI can be broken into two distinct processes: calculating a model that captures the geometry and physics of the cardiac electrical activity (the forward model) and the subsequent solution to a reconstruction or inverse problem based on that forward model. The forward model describes the distribution of body surface potential (BSP) signals given a particular representation of the cardiac bioelectric source. The inputs to the forward model are a mathematical model of cardiac electrical activity (the source model) and the geometries, conductivities, and relative positions of organs within the torso (the geometric model). The forward model then serves as the input for an inverse problem in which parameters of

Abbreviations: ECGI, Electrocardiographic Imaging.

* Corresponding author. 72 South Campus Dr. SLC, UT, 84112, United States.
E-mail address: jbergquist@sci.utah.edu (J.A. Bergquist).

https://doi.org/10.1016/j.compbiomed.2021.105174
Received 4 November 2021; Received in revised form 22 December 2021; Accepted 23 December 2021
Available online 20 January 2022

the source model are estimated given a specific set of BSP signals. This electrocardiographic inverse problem is an ill-conditioned estimation problem, meaning that the solutions are highly sensitive to small fluctuations or noise in the inputs or small errors in the model [14].

As noted above, cardiac position in the geometric model is a common and poorly controlled source of error in ECGI. Uncertainties in heart position arise inevitably due to respiration and shifts in body position [15,16]. They also arise as noise in the imaging modalities, typically MRI or CT, from which geometric models are derived. Images are usually captured during a single phase of the respiratory and cardiac cycles and often well before or after the ECGs are acquired. Thus the geometric models generated from the imaging do not account for cardiac position changes. Changes in cardiac position cause changes in the ECG signal morphology [17,18]. Our previous studies suggest that ECGI is very sensitive to the resulting errors in the geometric model, and incorporation of a corrected cardiac position can improve the ECGI solution [15,19]. Moreover, adjusting imaging protocols with forced "breath holds," respiratory gating, or rigid body restraints can be untenable in the clinical workflow. Even with accurate imaging, generating the associated time-varying heart position remains technically daunting. Hence there is a need for a method to automatically correct these forward model errors, ideally in a noninvasive manner.

A few methods for reconstructing cardiac position have been described in the literature. Svehlikova et al. proposed representing the electrical source activity of the heart as a single current dipole that approximates early activation of the cardiac septum [11]. They precomputed a range of candidate body-surface potentials from a collection of possible dipole positions and, finally, selected the cardiac position that produced the potentials that best matched measured values. This method was limited to correcting for translations only *i.e.,* not rotations of the heart, and relied on a limited number of precomputed solutions to define the search space. Rodrigo et al. proposed a less restrictive method for correcting errors in atrial geometries specifically by leveraging an observed behavior of a Tikhonov-regularized inverse solution. Their method was based on evaluating the sharpness of the L curve [13], which is a graph used in some regularized[1] inverse methods that results from plotting the inverse residual vs. the regularization cost on a logarithmic scale. They observed that the second derivative of the corner of this L curve, a measure of the 'sharpness' of the curve, increased when the atrial position was closer to the correct position. Consequently, their algorithm used this sharpness as a criterion for optimizing the cardiac position. This method is promising, and has seen ongoing development [20], but has only been applied to atrial geometries and with limited validation. Recently Toloubidokhti et al. applied machine learning techniques to correct for variability and errors in the forward model by leveraging a type of neural network known as a variational auto-encoder (VAE) [21]. They trained the VAE on a range of forward models, which included variation in the cardiac position. They then leveraged the structure of the VAE, which provides a compact parameterization of training data, to optimize for a forward model that minimizes ECGI error. This method showed promise in bridging machine learning techniques with traditional ECGI approaches, but to date only limited initial validation has been reported [21]. Coll-Font et al. proposed a method that minimized the residual between forward computed and measured body surface potentials by optimizing over a continuous range of cardiac positions [12]. This method also showed promising results, but in its initial implementation it required invasively measured electrograms, hence limiting its clinical applicability. Therefore, there remains a challenge to find a clinically tractable method that can estimate cardiac position accurately in the context of ECGI on a beat-by-beat basis.

[1] Regularization is a numerical technique needed to address the ill-posed nature of most inverse problems. This involves adding some weighted constraints to the formulation [14].

Here we propose an extension of the method introduced by Coll-Font et al. that allows for correction of the cardiac position within the torso without including measured electrograms; only body surface potential (BSP) recordings and a nominal static geometric model are required. We describe and validate this geometric correction framework using a range of synthetic datasets purposely designed to test its performance. The resulting method has the potential to improve ECGI solutions in both clinical and experimental contexts with minimal additional procedural and computational overhead.

2. Methods

Our geometric correction method leverages an iterative, alternating-minimization optimization framework that alternates between estimating beat-specific parameters of the forward model for multiple heartbeats and estimating the cardiac bioelectric source that is compatible with these heartbeats. We will first explain our optimization framework in a general form. Then we will describe how we have applied and tailored that general optimization framework to the task of estimating cardiac position in our specific setting.

2.1. Optimization framework

The optimization framework in this study assumes that the following inputs are available:

- a parameterization of some aspect of the forward model to be optimized, *e.g.,* cardiac position defined as both translation and rotation of the heart.
- BSP measurements from a number of heartbeats for which to optimize the parameterization of the forward model. The number of heartbeats must be more than one.
- a model of the cardiac sources, *e.g.,* epicardial potentials.
- a geometric model of the torso which includes the body surface, the heart, and any other organs of interest.
- a computational algorithm that takes in the geometric model to produce a forward solution, specifically a forward matrix that can approximate body-surface potentials given a corresponding description of the source model.

As noted, our optimization framework operates using a number of heartbeats, $K > 1$. We represent the parameters of the forward model for the k'th heartbeat as the $L \times 1$ vector $\mathbf{p}_k$ where L is number of parameters used in the parameterization of the forward model. We collect the parameters for all K $\mathbf{p}_k$ vectors in a $L \times K$ matrix $\mathbf{P}$. We represent the BSP measurements for any specific beat as the $m \times t$ matrix $\mathbf{B}_k$ where m is the number of recording electrodes on the torso surface and t is the number of time instances in a beat. (The optimization framework assumes that t is the same for all K heartbeats, see 2.3.) We represent the single beat of cardiac sources as the $n \times t$ matrix $\mathbf{H}$ where n is the number of reconstruction locations in the cardiac geometry. We represent the forward matrix for a specific heartbeat k as the $m \times n$ matrix $\mathbf{A}_k$. Note that $\mathbf{A}_k$ is a function of $\mathbf{p}_k$.

The optimization framework is based on an extension of a Tikhonov inverse solution formulation, which we have described previous as a 'joint inverse' formulation [19]. This joint inverse formulation estimates a single cardiac source by combining BSP measurements and forward matrices from multiple heartbeats. We combine the BSP matrices and forward matrices for all K heartbeats by concatenating them into the block matrices $\overline{\mathbf{\Phi}}$ and $\overline{\mathbf{A}}$ as shown below, where the overline denotes these as the joint matrices.

$$\overline{\mathbf{\Phi}} = \begin{bmatrix} \mathbf{B}_1 \\ \mathbf{B}_2 \\ \mathbf{B}_3 \\ \cdots \\ \mathbf{B}_k \end{bmatrix}$$

$$\overline{\mathbf{A}} = \begin{bmatrix} \mathbf{A}_1 \\ \mathbf{A}_2 \\ \mathbf{A}_3 \\ \cdots \\ \mathbf{A}_k \end{bmatrix}$$

Our overall objective function is given in Equation (1), below. The matrix $\mathbf{R}$ is a $n \times n$ Tikhonov regularization operator used to combat the ill-posedness of the inverse problem. R can take many forms, for example an identity matrix (zero-order regularization), a gradient operator (first-order regularization), or a Laplacian operator (second-order regularization). This regularization term is weighted according to the scalar λ.

We solve the optimization problem in Equation (1) by alternating between two steps. We denote each iteration of this alternation between steps 1 and 2 with the superscript q. In step 1, we estimate a single cardiac source $\mathbf{H}^q$, given $\overline{\mathbf{\Phi}}$ and the present estimate of $\overline{\mathbf{A}}^{q-1}$ which is a function of the most recent estimate of the forward parameters $\mathbf{P}^{q-1}$. In step 2 we estimate forward model parameters $\mathbf{P}^q$, given an estimate of the cardiac source from step 1, $\mathbf{H}^q$.

$$\arg\min_{\mathbf{P},\mathbf{H}} \|\overline{\mathbf{\Phi}} - \overline{\mathbf{A}}\mathbf{H}\|_2^2 + \lambda\|\mathbf{R}\mathbf{H}\|_2^2 \tag{1}$$

The two steps in this alternating minimization function as follows:

Step 1 Estimation of the cardiac source.

When estimating the cardiac source for the current iteration, $\mathbf{H}^q$, we fix the values for the forward model parameters $\mathbf{P}^{q-1}$. During the first iteration ($q = 0$) the values of $\mathbf{P}^{-1}$ are initialized at values that correspond to a nominal cardiac position; in subsequent iterations, the values of the forward model parameters are determined by the preceding parameter-estimation step $\mathbf{P}^{q-1}$ (see **Step 2**). With the values of $\mathbf{P}^{q-1}$ fixed, we estimate $\mathbf{H}^q$ using the 'joint inverse' formulation by solving the Tikhonov inverse problem shown in Equation (1).

Step 2 Estimation of the forward model parameters

When estimating the forward model parameters for the current repetition $\mathbf{P}^q$, we fix the values of the cardiac source estimate $\mathbf{H}^q$ to their values from the preceding cardiac-source estimation step. The algorithm estimates the forward model parameters $\mathbf{p}_k^q$ for each of the K recorded heartbeats using an interior points optimization algorithm (specifically, the non-linear constrained optimization algorithm implemented in the MATLAB 2020 fmincon function) for the objective function Equation (1) [12]. Since the objective function is separable given a fixed $\mathbf{H}^q$, the optimization can be performed in parallel for each heartbeat. This optimization in Step 2 is also iterative, and the number of steps selected is an additional hyperparameter of our overall optimization framework.

Once this optimization in Step 2 is complete, we fix the forward model parameters $\mathbf{P}^q$ and return to step 1 to solve for the next iteration of $\mathbf{H}^{q+1}$ with the new forward model parameters. We continue to alternate between Steps 1 and 2 until the estimated forward model parameters converge, defined as a change in the Frobenius norm of the difference between $\mathbf{P}^{q-1}$ and $\mathbf{P}^q$ less than a threshold or when a maximum repetition count is reached.

2.2. Implementation

We implemented this optimization scheme under the following specific conditions relevant to the task of reconstructing cardiac position, including a cardiac bioelectric source model, position parameterization, and appropriate numerical and computational methods.

Cardiac source model: The source model consisted of the electric potentials on a surface constructed from a cage of electrodes that surrounded the isolated heart in the experimental model described below.

Parameterization of the Forward Model: The forward model was based on a homogeneous volume conductor of the space between the heart and body surfaces, with all other organs omitted, both for simplicity and because it replicated the experimental setup used to gather validation signals (described below). The forward model parameters $\mathbf{P}$ in this case described changes in the cardiac position for every heartbeat— *i.e.,* translations and rotations of the heart. We parameterized the positions of the heart with 6° of freedom ($L = 6$), as in our previous studies([12]). Translations were along the x-axis, the left-right direction of the torso geometry, the y-axis, anterior-posterior, and the z-axis vertical, following the well-accepted conventions of the EDGAR database for geometric models [22]. Rotations were specified as combinations of pitch, yaw, and roll, where pitch was rotation of the septal axis of the cardiac geometry about the Y axis, yaw was rotation of the septal axis about the X axis, and roll was rotation of the cardiac geometry about the septal axis (see Supplemental Video s.2).

Computational implementation details: In Step 1 of the minimization we find a single regularization parameter across all t time samples, using the L-curve criterion. We refer to this method of regularization as the Frobenius L-curve criterion.

Step 2 consisted of estimating the heart position with a maximum of 10 steps of interior-point optimization for each new position parameter, with the goal of avoiding overfitting of the position parameters on any single estimate of the cardiac source. We also imposed constraints on the cardiac position by including box constraints on its parameters to force them to be within the following ranges: 0.4 to 0.4 radians for pitch, and yaw, −0.9 to 0.9 for Roll, and −25 to 25 mm for x, y, and z position. These bounds reflected the bounding box in which the cardiac geometry (described below) could fit within the torso geometry without contact between them.

Fig. 1 shows a schematic representation of our geometric correction framework. The stopping criterion for our implementation of the described algorithm was iteration count, which we set to 50 iterations for all experiments. We observed convergence of the position parameters within 20–40 iterations across all cases. Other stopping criteria based on convergence of the estimated cardiac position parameters could also easily be implemented.

Software and computational resources: The geometric optimization and inverse solutions were computed using a combination of custom software created in MATLAB (Mathworks Inc, Natick, MA) and the SCIRun Forward/Inverse Toolkit (SCI Institute, University of Utah) [23]. Visualizations were generated using MATLAB functions and SCIRun modules. All optimizations were computed using the computational resources at the Scientific Computing and Imaging (SCI) Institute at the University of Utah, Salt Lake City, Utah, USA.

2.3. Datasets

To evaluate the geometric correction framework required data in which the cardiac position, BSP signals, and electrograms (EGMs) were known for a series of heartbeats. To achieve these specific requirements, we generated a set of partially synthetic electrocardiographic signals derived from measured geometry and experiments with a large-animal model.

Electrocardiographic Signal Acquisition and Processing: The source of geometry and electrocardiographic signals for this study was an isolated-heart preparation described in Bergquist et al. [10,24]. All details of the study were approved by the University of Utah IACUC (Protocol #17-04 016). Briefly, an isolated, perfused canine heart was suspended in a torso-shaped fiberglass tank filled with an electrolyte

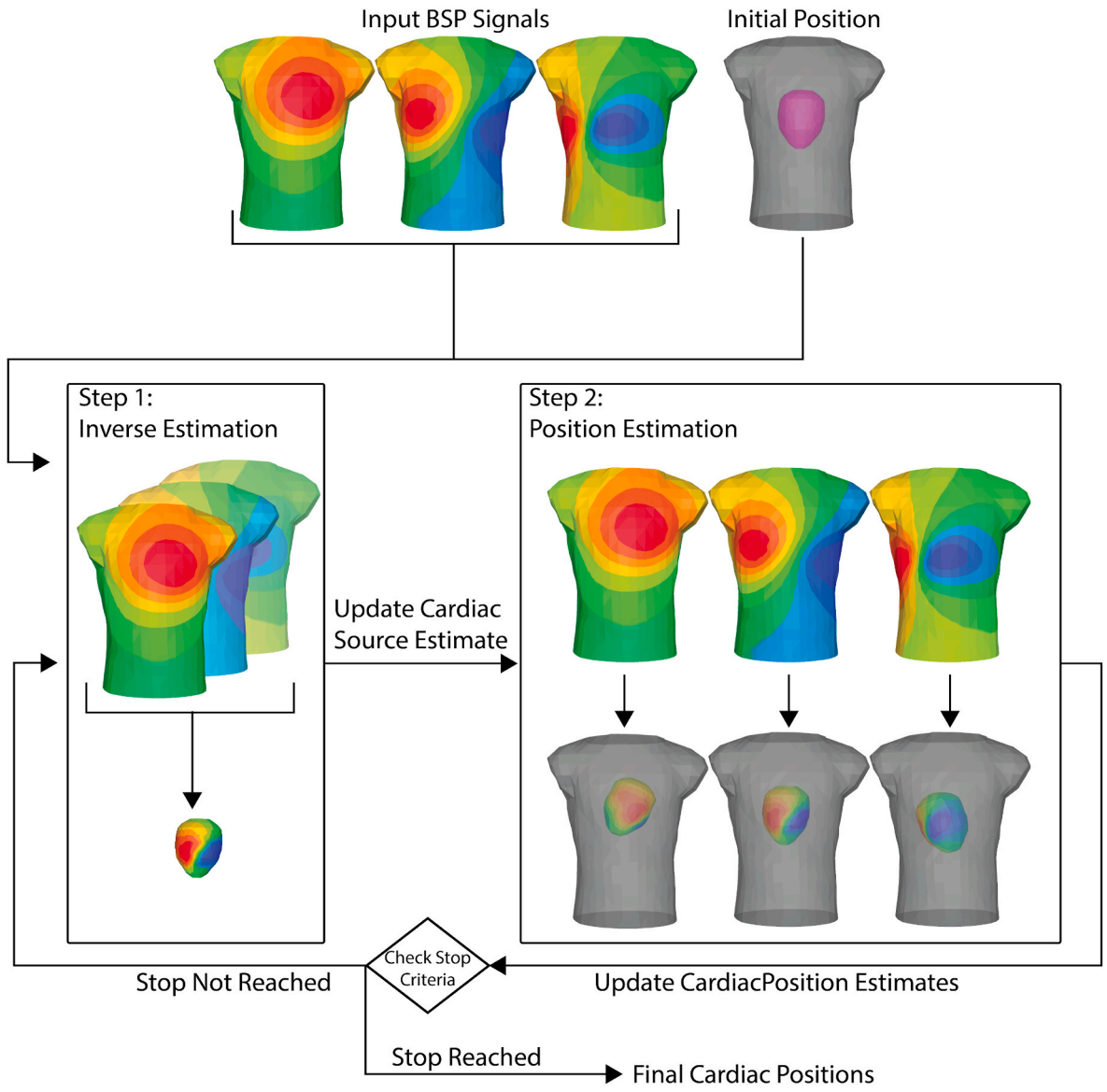

Fig. 1. Schematic representation of the geometric optimization algorithm. Initially BSP signals and a starting cardiac position are supplied for each heartbeat. In our case, the same cardiac position was supplied initially for all heartbeats. During step 1, the 'joint inverse' method is used to estimate cardiac surface potentials using all BSP signals and cardiac positions. In step 2 the estimated cardiac surface potentials are used to estimate new cardiac positions individually for each heartbeat. After Step 2, the stopping criteria is evaluated. In this study, the stopping criteria was iteration count, set to 50. The output from step 2, a new set of estimated cardiac positions, is either fed back into step 1 for the next iteration or passed as the output.

solution approximating the conductivity of the human torso (500 Ω·cm). Fig. 2 describes the setup, which included a heart that was instrumented with a variety of recording arrays including a 256-electrode Utah Pericardiac Cage (UPC) ($n = 256$ from the description above). The UPC was a 3D-printed plastic, two-part frame into which 256 Ag/AgCl electrodes were embedded. The electrodes encircled the isolated heart roughly 1–2 cm from the epicardial surface. Electrode spacing was consistent over the surface and electrode locations formed a triangulated surface with an average area of 84 mm^2 and an edge length of 21 mm. The electrodes provided continuous sampling during sinus rhythm and during stimulated ectopic beats paced from the anterior left ventricle (VP, ventricularly paced). Signals were captured using a custom acquisition and multiplexing system described in Zenger et al. [25], which included amplifiers, filters, and analog to digital converters. The recorded signals were then baseline corrected, noise filtered, and segmented into individual beats using PFEIFER, an open-source software tool for processing time series data from electrocardiographic experiments [26]. A representative heartbeat (QRST) was segmented from the series of recorded beats for each of the two activation sequences (sinus and anterior VP), which we refer to in the sequel as sinus and aVP, respectively. These recordings represent our ground truth cardiac sources, **H**.

Additionally, we sought to evaluate the impact of biological, beat-to-beat variation on algorithm performance. To that end, we applied PFEIFER's auto-segmentation algorithm to segment an additional 39 similar beats from a continuous recording based on the aVP template; these beats corresponded to a temporal correlation cutoff of 0.98 between template and subsequent beats, thus they formed a train of similar, but not identical, beats. These beats, including the template (totaling 40 beats), will be referred to as aVp1–40. These 40 beats were then normalized to all have 360 time samples per QRST (*i.e.,* $t = 360$) using temporal resampling with cubic splines fit to each electrogram. The result was a matrix of 256 × 360 values for each of the aVp1–40 heartbeats.

Computational Model Generation: The first step to create our computational models was to generate a geometric model based on the torso-

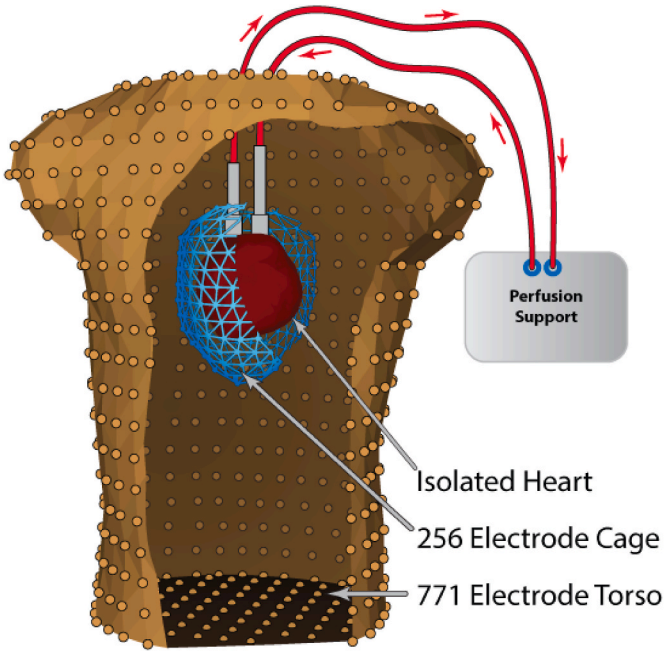

Fig. 2. Experimental setup used to generate geometric model and electrocardiographic signals. The Utah Pericardiac Cage (blue) recorded signals from near the heart surface during sinus and anterior left ventricular pacing. The UPC geometry was registered post experiment into the 771-node torso-tank geometry. This visualization shows part of the torso tank and UPC cut away to illustrate relative positioning.

tank and the Utah pericardial cage (UPC). The triangulated surfaces from both the tank surface and the cage electrodes have been previously meshed and with a model based on surface (rather than volumes) all that was needed to was to locate the UPC within the torso, which we measured using a mechanical digitizer (Microscribe, Immersion Corporation) during the experiment. Fig. 2 shows the resulting model, which contained 771 nodes to represent the torso surface (m) and 256 pericardial nodes to represent the cardiac geometry (n). As the anchor point for the cardiac geometry we defined the centroid of the electrode positions in the top quarter of the UPC, an approximation of the atrial region of the heart. The septal axis was defined as the vector between this atrial anchor point and the equivalent centroid of the electrodes in the lower three quarters of the UPC, equivalent to the ventricular region.

To simulate respiratory motion of the heart, we numerically moved the cardiac geometry within the torso according to two types of motion: translations in x, y, and z directions and three rotations: pitch, yaw, and roll, as defined above. We treated the resulting cardiac positions as the targets that we subsequently attempted to reconstruct. The respiratory cycles were parameterized by a phase value between 0 and 1, sampled 100 times using a sinusoidal function. We then applied these respiratory phase values to each of the, x, y, z, pitch, yaw, and roll values linearly over the ranges defined in Table 1. This first collection of positions (position set 1, $K = 100$) spanned almost the entire torso, which

Table 1
Ranges for the parameter values for each position set. Ranges are represented with min, max. For each position, a sample was taken of the respiratory phase value (0–1) and used to calculate the six parameter values (pitch, yaw, roll, X, Y, Z) for that position by scaling that value to each of the parameter ranges.

Position Set	Pitch (Rad)	Yaw (Rad)	Roll (Rad) 0	X (mm)	Y (mm)	Z (mm)
Set 1, 3, and 4	−0.35, 0.35	−0.35, 0.35	−0.79, 0.79	−20, 20	−20, 20	−20, 20
Set 2	-.022, 0.35	−0.024, 0.19	−0.002 4, 0.000 2	−0.66, 0.41	0.22, 1.15	−22.49, 1.82

Table 2
Simulated datasets along with leadsets evaluated. For each position set, cardiac positions were reconstructed using each of the specified activation sequences and leadsets. Limited 1:12 leadsets correspond to the 12 leadsets shown in Fig. 4 whereas the full leadset used the potentials at all of the torso node locations.

Position Set	Activation Sequences	Leadsets	Number of Cases
Set 1	Sinus, aVP, aVP1:40	Full, Limited 1:12	39
Set 2	Sinus, aVP, aVP1:40	Full, Limited 1:12	39
Set 3	aVP	Full	100
Set 4	aVP	Full	1

exaggerated normal respiratory motion. The second position set was more physiological (position set 2, again $K = 100$), based on fitting the pitch, yaw, roll, x, y, and z ranges to the those of a human heart during free breathing recorded via magnetic resonance imaging (MRI) of a single subject at multiple positions and phases of the breathing cycle, as described previously [15]. Fig. 3 visualizes the changes in cardiac position for each of these two position sets. Finally, to test the response of our algorithm to variation in the set of target positions, we generated 100 realizations of 100 positions randomly sampled along the respiratory phase across the same range as for position set 1. The collection of 100 instances of 100 positions will be referred to collectively as position set 3. During geometric optimization, each realization of 100 positions from position set 3 was optimized separately such that $K = 100$ in each case (see Table 2).

The pericardiac cage is larger than a typical heart. To investigate what effect a smaller target cardiac geometry might have we shrunk the cage geometry by scaling it down 25% with respect to the center of the geometry. We then generated 100 positions of the smaller cardiac geometry as described above, using the parameter range and sampling for Position Set 1. We refer to theses positions as Position Set 4.Table 1 contains the ranges for the 6 parameters for all position sets.

To summarize, we considered four sets of cardiac positions as versions of ground truth and set out to recover these positions based only on the torso potentials generated from a cardiac, bioelectric source located there (details of the torso potentials follow below). Set 1 consisted of 100 cardiac positions sampled from a large range of motion. Set 2 consisted of 100 cardiac positions sampled from a physiological range based on the measured respiratory motion of a single human subject, and Set 3 consisted of 10,000 positions(in groups of 100) determined by randomly sampling the respiratory phase. Set 4 consisted of 100 cardiac positions sampled from a large range of motion using a small cardiac geometry. When performing the geometric optimization, we initialized the cardiac position to the original registered location, corresponding to the zero-values of all six parameters.

Generation of BSPs: For each of the geometric models described above, we calculated the associated forward transform matrix that maps pericardial to torso potentials using the boundary element method, a well characterized approach in ECGI [27,28]. These forward matrices were then used to generate synthetic BSPs for each cardiac position. To capture some biological and measurement variability, we added white Gaussian noise at a signal-to-noise ratio (SNR) of 30, applied independently to each BSP signal. No subsequent filtering or signal processing was performed on the BSP signals before use in our algorithm. For Position Sets 1 and 2, three sets of BSPs were generated: one used the sinus beat ($K = 100$), one was based on the ventricularly paced beat ($K = 100$), aVP, and the third was generated by applying the sequence aVP1 through aVP40 as the source EGMs for the first through fortieth cardiac positions in each position set ($K = 40$). For Position Sets 3,and 4, the same aVP beat was used throughout.

Leadsets: To evaluate the response of our method to limited sampling of the torso surface, we designed twelve reduced leadsets, summarized in Fig. 4. Combined with the full leadset, this made for thirteen different samplings of torso potentials. For Position Sets 1 and 2, we performed geometric optimization using all thirteen leadsets and all three sets of

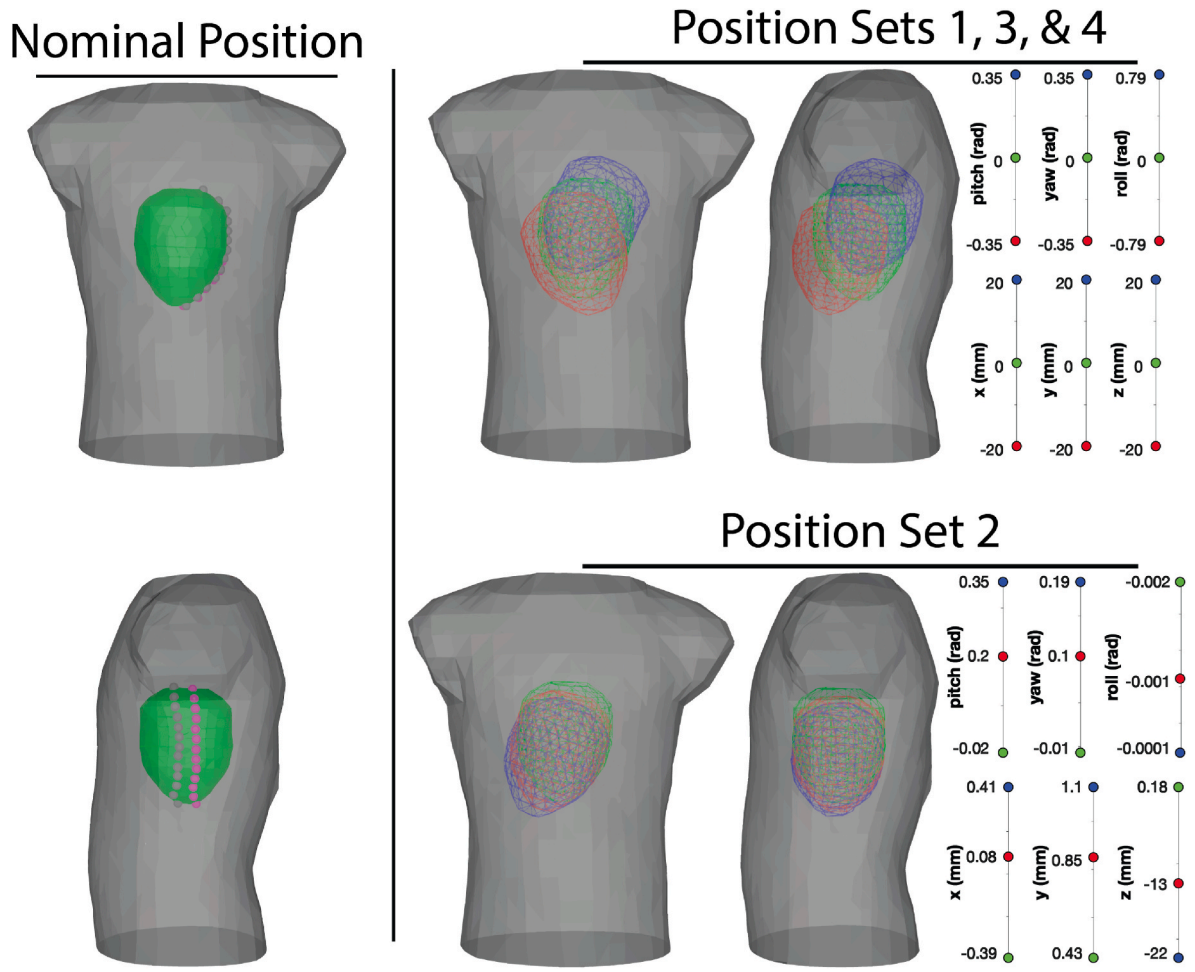

Fig. 3. Demonstration of the cardiac position ranges for each position set. The cardiac geometry in the nominal position (green) on the left column is moved to positions within each of the ranges defined for Position Sets 1, 2, 3, and 4. The right panels show example cardiac positions in those parameter ranges, with position parameters shown in the accompanying plots. Note that Position Sets 1, 3, and 4 use the same range. The two views of the torso show the anterior view and the left side view. The color of the cardiac geometry corresponds to the colored dots on the parameter graphic. The cardiac geometry is shown using a wire-frame model to allow for simultaneous visualization of the overlapping positions. Position Set 2 covers a substantially smaller range of motion than Position Sets 1, 3 and 4. The colored nodes (pink and gray) on the nominal geometry indicate the region of the cardiac geometry that is cut when the geometry is flattened for subsequent visualizations. This cutting and flattening process can be seen in Supplemental Video s.1.

BSPs, resulting in six reconstruction scenarios (two position sets * three BSP sets) for each of those thirteen leadsets. For Position Set 3, we utilized only the full leadset, resulting in 100 reconstruction scenarios. For Position Set 4 we utilized only the full leadset resulting in 1 reconstruction scenario.

2.4. Performance analysis

We assessed the performance of our geometric correction framework both for its ability to reduce geometric error as well as to improve the accuracy of individual ECGI inverse solutions.

Geometric error: Geometric error was assessed both as the error between reconstructed and target cardiac position parameters and also the resulting average position error between target and optimized cardiac geometries. For the latter we calculated the mean distance between the corresponding nodes of the reconstructed and target geometries. We made a distinction between parameter reconstruction and position reconstruction because each captured a different facet of the error. We also carried out visual evaluation of the differences between reconstructed and target geometries.

During our analysis we also found a need to differentiate between the accuracy of geometric reconstruction and the precision of geometric reconstruction. Our geometric correction method solves for the cardiac position for a group of heartbeats, ideally estimating these positions as closely as possible to the target positions. Because this estimation operates on a group of heartbeats we may consider their positions relative to one another, that is how the position of the cardiac geometry for each heartbeat relates to the cardiac position of every other heartbeat which we refer to as the precision of the reconstruction. On the other hand, the accuracy refers to how the optimized cardiac geometry for one heartbeats relates to the target cardiac geometry for that same heartbeat. Ideally we would like our algorithm to have high accuracy and precision, reconstructing both the relative cardiac positions with respect to each other, and the absolute cardiac positions with respect to their target positions. We evaluated the accuracy and precision both visually with respect to the position parameters and through the per-electrode localization error metric.

ECGI accuracy: To assess the improvement in reconstructions of the heart potentials, we computed ECGI solutions using the non-optimized, optimized, and target geometries across all positions and beat morphologies for each BSP signal. For these computations, we implemented a standard Tikhonov inverse solution with second-order regularization to solve the inverse problem [28]. For each inverse solution, the Frobenius L-curve criterion (described above) was used to select the regularization weight, λ for each beat. The entire QRST duration of the signal and the full leadset were utilized for reconstruction.

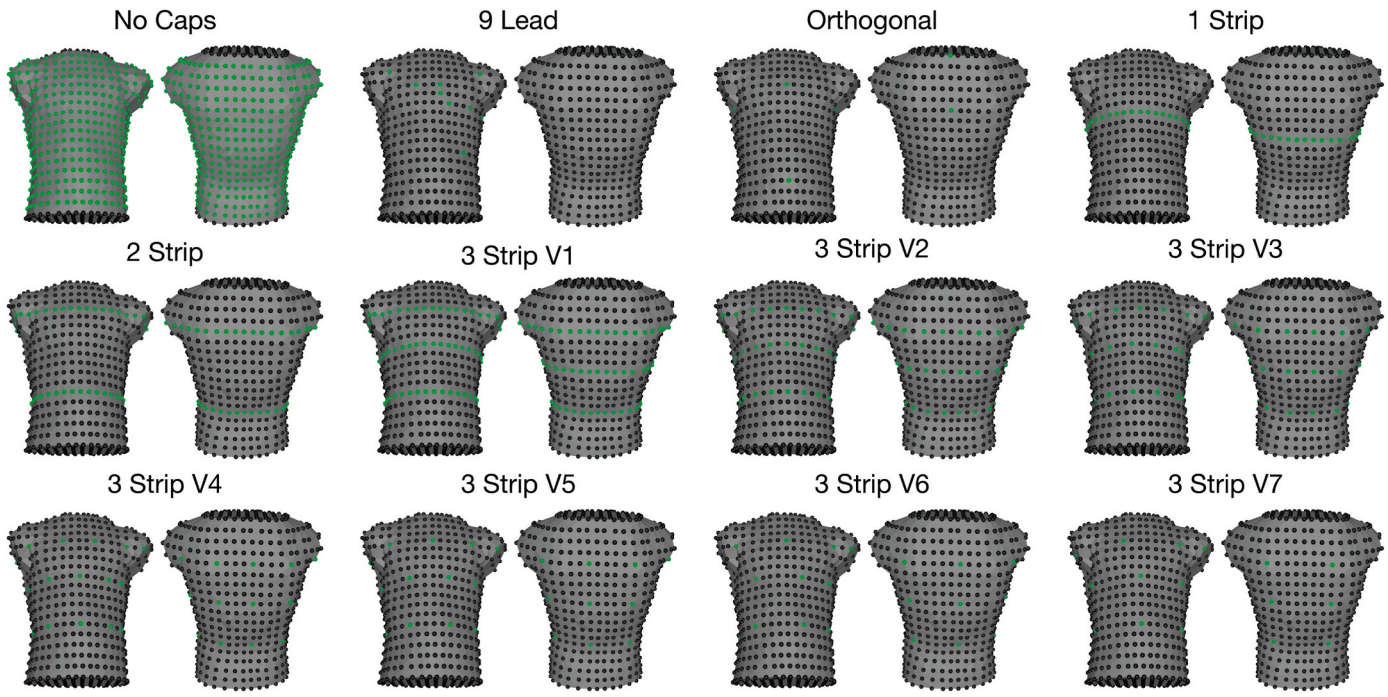

Fig. 4. Sub-sampling of the torso BSP signals. Spheres represent electrode recording locations and the green spheres highlight the electrodes included in each leadset. Leadsets were designed to explore a range of sampling scenarios. The 'no caps' leadset represents removing the electrodes from the torso that make up the top and bottom of the torso mesh, which would be unrealistic to sample from in a clinical implementation. The leadsets called '3 Strip' versions 1 to 7 (V1–V7) represent successive downsampling of the same three strips of electrodes around the circumference of the torso. The full leadset (the entire set of spheres shown in each diagram plus a grid of electrodes added to the top and bottom) used all nodes on the torso surface. Number of electrodes per leadset: Full: 771, No Caps: 596, 9 Lead: 9, Orthogonal: 6, 1 Strip: 34, 2 Strip: 72, 3 Strip V1: 106, 3 Strip V2: 53, 3 Strip V3: 37, 3 Strip V4: 28, 3 Strip V5: 22, 3 Strip V6: 19, 3 Strip V7: 16.

The resulting estimated EGMs were compared to corresponding ground truth values using several metrics described previously [24]. Specifically, we calculated the root-mean-squared error (RMSE) over the QRST between reconstructed and ground truth EGMs, the mean temporal correlation (TC) (*i.e.,* the correlation of reconstructed vs. ground-truth EGMs over the QRST on an electrode by electrode basis averaged across all electrodes), and the mean spatial correlation (SC) (*i.e.,* the correlation between cardiac surface potential distributions averaged over all time instances in the QRST). Finally we visually compared the potential maps of the reconstructed and ground-truth values.

3. Results

The products of our optimization were twofold, geometric error and the quality of the ECGI reconstruction, and each perspective provides separate insight into the success and utility of this approach.

3.1. Geometric reconstruction error

Position Sets: Fig. 5 shows the position parameter reconstruction and per-node localization errors for Position Sets 1 (top) and 2 (bottom) using the full leadset and aVP activation sequence. The scatter plots for the parameter reconstructions have the target parameter value along the X axis and the reconstructed parameter value along the Y axis. The solid black lines show the target parameter line and the solid red lines show the initialized parameter values. The black diamonds are the reconstructed parameters for each beat in the position set. Thus, any deviation of the black diamonds from the solid black line indicates the error in the parameter reconstruction. The panels on the right side display box plots of the per-node localization error with respect to the target positions for both the optimized and non-optimized cardiac geometries. We plot the non-optimized per-node localization error as a comparison to the optimized which shows the degree to which the optimization was able to reconstruct heart position.

Table 3 summarizes numerically the per-node localization error for position sets 1 and 2 with the full lead set across all activation sequences. Table 4 shows the per-node localization error for Position Set 3, averaged over all beats from all 100 realizations ($k = 10{,}000$). In Table 4 we summarize the ECGI reconstruction statistics for Position Set 3, discussed below in Section 3.2.

The error in cardiac position reconstruction varied across position sets, with Set 4 producing the lowest error. As shown in Fig. 5, the reconstructed position parameters more closely matched the target line for the X, Y, and Z positions than the rotations, especially in Position Set 1. The parameter reconstruction accuracy and localization error did not vary substantially between Position Set 1 and 3, as shown in Table 4. The geometric reconstruction error for Position Set 4 was lower than Position Set 1, as shown in Table 4. The parameter reconstruction accuracy was similar between position sets 1 and 4, as shown in Supplemental Fig. 5. Position Set 2 showed higher overall geometric reconstruction error than the other position sets. However, for Position Set 2 we noted that often the relative parameters, *i.e.,* the trend of position parameters and their relative values between beats as discussed in Sec. 2.4, appeared to be well reconstructed, but with an offSet. This trend is most apparent in the pitch and the X shift for Position Set 2 as seen in Fig. 5. The slope of the reconstructed parameters visually matches the target line, but the reconstructed values are offset from the ground truth by what appears to be a consistent value. Such results suggest that while the precision of the reconstruction was high, the accuracy was not. The precision of reconstruction is also reflected by the preservation of cardiac geometry as indicated by the very tight distribution of per electrode localization error in Fig. 5.

Activation Sequences: Fig. 6 shows the mean per-node localization error between the target geometries and the optimized geometries for each activation sequence along with the starting errors for the non-optimized geometries. The optimized positions depicted in Fig. 6 used

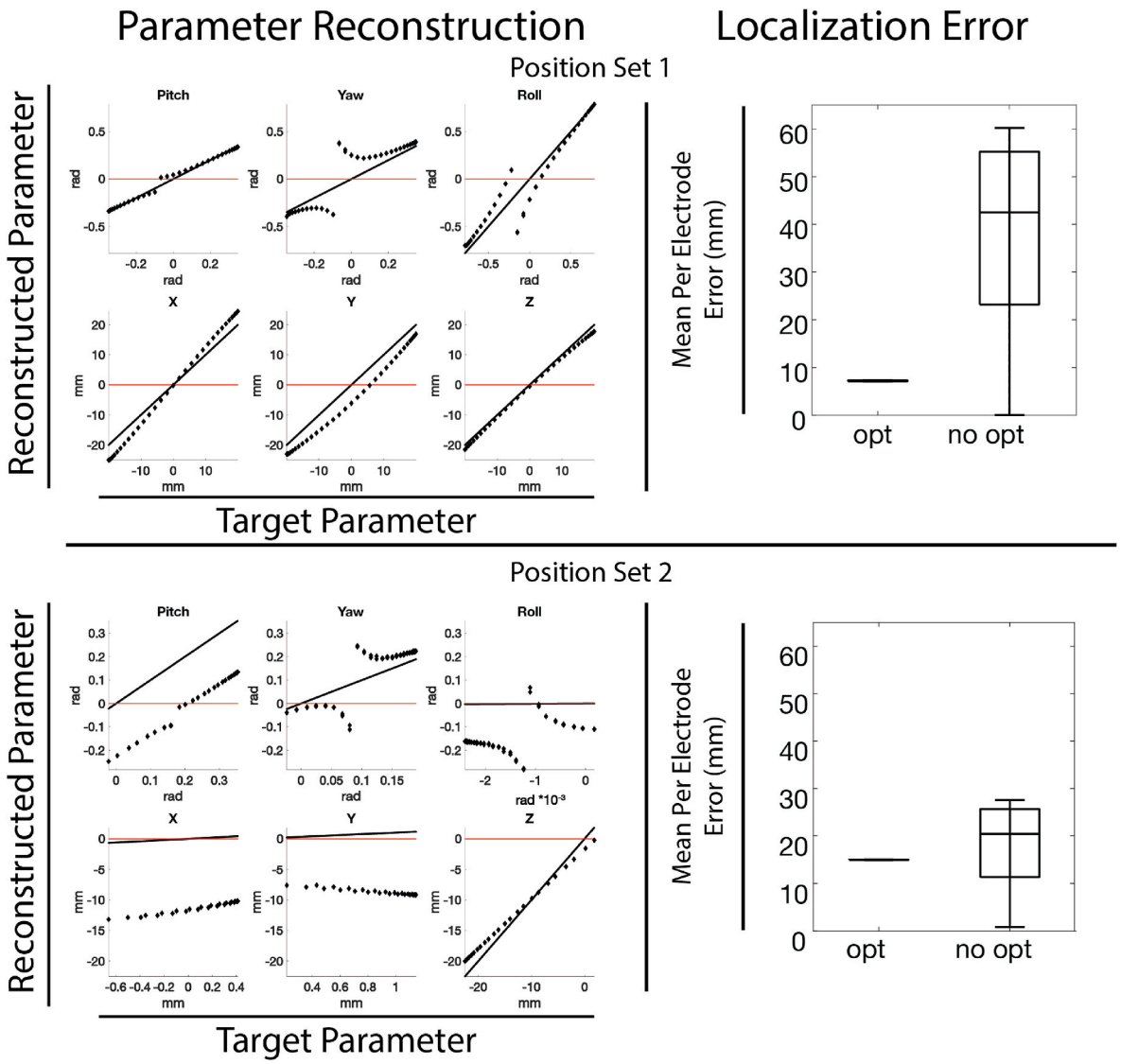

Fig. 5. Reconstructed parameters and mean per-electrode localization errors for Position Sets 1 (top) and 2 (bottom). The scatter plots (left) capture parameter reconstruction errors, in which the red line indicates the initial parameter values, the solid black line shows the target cardiac position parameters, and the diamonds show the reconstructed parameters. Note the change in scaling of some the of plots to facilitate interpretation of the parameter reconstructions, which sometimes had very different ranges, such as in Position Set 2. The right plots show box plots across all positions of the per-node localization error (mm) between optimized and non-optimized cardiac positions.

Table 3
Average per-node localization error (in mm) across each Position Set and activation sequence for the full leadset. Values are shown as means ± one standard deviation.

	Position Set 1	Position Set 2
aVp	7.18 ± 0.09	15.00 ± 0.05
sinus	6.41 ± 0.08	14.72 ± 0.05
aVp1:40	8.97 ± 2.05	17.02 ± 2.96

the full leadset and Position Set 1. As before, the non-optimized per-node localization errors provide a reference of the initial placement of the cardiac geometry before optimization. Geometric reconstruction errors varied across activation sequences, with sinus showing slightly less error for both parameter reconstruction and per-electrode localization. The aVP1-40 Position Set, which incorporated beat to beat variability among EGMs, showed slightly higher errors in per-electrode localization than aVP alone as seen in Table 3, and also in parameter reconstruction (see Supplemental Fig. 1).

Table 4
Cardiac localization error and ECGI accuracy for Position Set 3. Averages and standard deviations were taken over all 10,000 positions (100 positions from 100 realizations). Mean per-electrode localization error (Loc. Err.) is in millimeters and root-mean-squared error (RMSE) is in millivolts. Spatial correlation (SC) and temporal correlation (TC) are scaled between −1 and 1. Values are shown as means ± one standard deviation.

Stat	Value
Loc. Err	8.51 ± 0.97 mm
RMSE	0.34 ± 0.02 mV
SC	0.94 ± 0.01
TC	0.95 ± 0.01

LeadSets: Fig. 7 reports the per-node localization error between the target geometries and the optimized geometries for each leadset along with for the starting error for non-optimized geometries. Results are

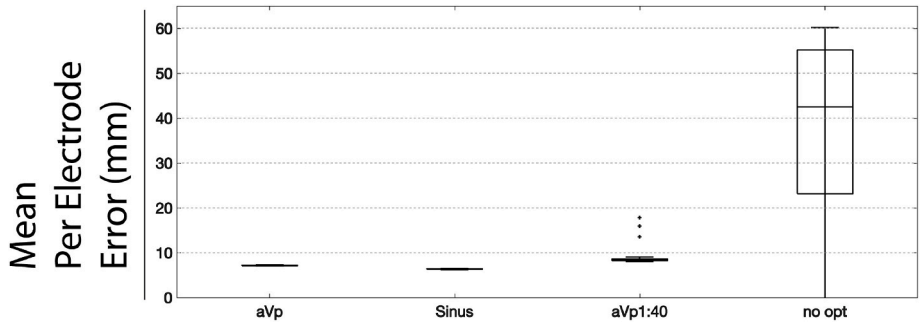

Fig. 6. Mean per-node localization error across the three activation sequences for Position Set 1. These results used the full leadset. The non-optimized errors are shown on the right for comparison. Plus signs denote outliers, defined as a value that is more than 1.5 times the interquartile range away from the bottom or top of the box.

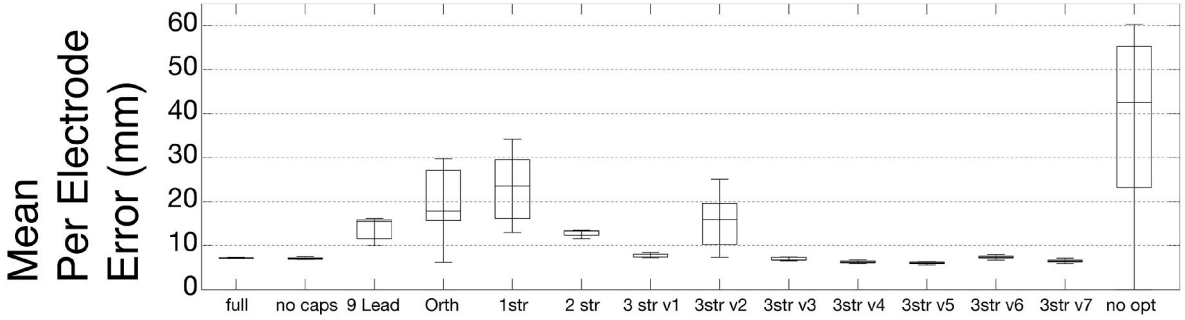

Fig. 7. Box plots of mean per-node localization error across the different leadsets for Position Set 1 and the aVp activation sequence. The leadset names correspond to those shown in Fig. 4 (full: Full lead set, no caps: no caps leadset, 9 lead, 9 lead leadset, Orth: Orthogonal, 1 str: 1 strip, 2 str: 2 strip, 3 str v1:7, 3 strip version 1 to 7. No opt: non-optimized position). The full leadset uses all nodes of the torso mesh.

based on the aVP activation sequence and Position Set 1. Parameter reconstruction error increased as leadset sampling density decreased (see Supplemental Fig. 3). However, increased parameter reconstruction error did not always result in increased per-electrode localization error, as shown in Fig. 7. Generally, as sampling density decreased, the reconstruction of the position parameters X, Y, and Z showed higher errors than those of the rotation parameters (Supplemental Fig. 3). We observed that the smallest leadsets (9 lead, orthogonal, 1 strip, 2 strip) resulted in large reconstruction errors of X, Y, and Z translations, and less severe errors in pitch, yaw, and roll, which varied based on the specific leadset (Supplemental Fig. 3). Notably, several of the reduced leadsets (3-strips v3 through v7) showed per-electrode localization error comparable to the full leadset despite increases in parameter reconstruction error.

3.2. ECGI accuracy

Position Sets: The box plots in Fig. 8 show the ECGI accuracy between Position Set 1 and 2 using the optimized, target, and non-optimized cardiac positions. The optimized geometries used to generate the inverse solutions for Fig. 8 were found using the full leadset and the aVP activation sequence. Each row depicts a different statistic computed between the ECGI solutions for each cardiac position and the ground truth aVP EGM.

Table 7 shows the average values for each of the three ECGI accuracy metrics (RMSE, SC, TC) ± one standard deviation for Position Sets 1 and 2.

Fig. 9 shows spatial comparisons of best and worse case ECGI solutions in terms of potential maps for non-optimized position (on the left), optimized position (middle), and target position (right) for the parameter Sets 1 and 2 and the aVp activation sequence. The potential maps are shown on a flattened version of the pericardiac cage. This flattened version was created by cutting down a vertical strip on the cage geometry along the left midaxillary line, as indicated in Fig. 3 by the colored spheres. The resulting flattened geometry is centered on the right midaxillary line. Supplemental video s.1 shows this flattening. All potential maps are shown at a time point corresponding to the maximum of the root mean squared signal of the measured EGM, depicted in the bottom right section of the figure. The best case beat is defined as the beat with the maximum spatial correlation of the reconstruction potentials compared to ground truth potentials using the optimized geometries while the worst case beat is defined as the beat with the minimum spatial correlation of the reconstruction potentials compared to ground truth potentials using the optimized geometries. We show the measured EGM in the bottom left section of the figure. Rows one and two show the best and worst case reconstructions for Position Set 1 respectively, rows three and four show the same for Position Set 2. The RMSE (in mV), SC, and TC for each ECGI solution are shown above the corresponding potential map. Supplemental Fig. 4 shows the potential maps in the same arrangement for the sinus activation sequence.

Table 6 shows the percent of heartbeats for each testing scenario in which geometric optimization resulted in improvement according to each of the metrics.

Across all metrics the ECGI reconstructions were improved for the majority of heartbeats by geometric optimization for all position sets except for position set 2 using the Sinus activation sequence (see Table 6). Often the accuracy seen after geometric optimization approached the accuracy seen using the target positions. ECGI improvements were more modest for Position Set 2, as shown in Fig. 8 and Supplemental Fig. 21. For Position Set 3, ECGI accuracy showed a slightly higher variability than in Position Set 1, reflected in a higher standard deviation of the ECGI accuracy metrics shown in Table 4. Despite this increased variability in ECGI accuracy, Position Set 3 still demonstrated notable improvement in ECGI accuracy over the non-optimized solutions. Position set 4 showed higher RMSE and slightly lower correlation values than Position Set 1, as shown in Table 5 and

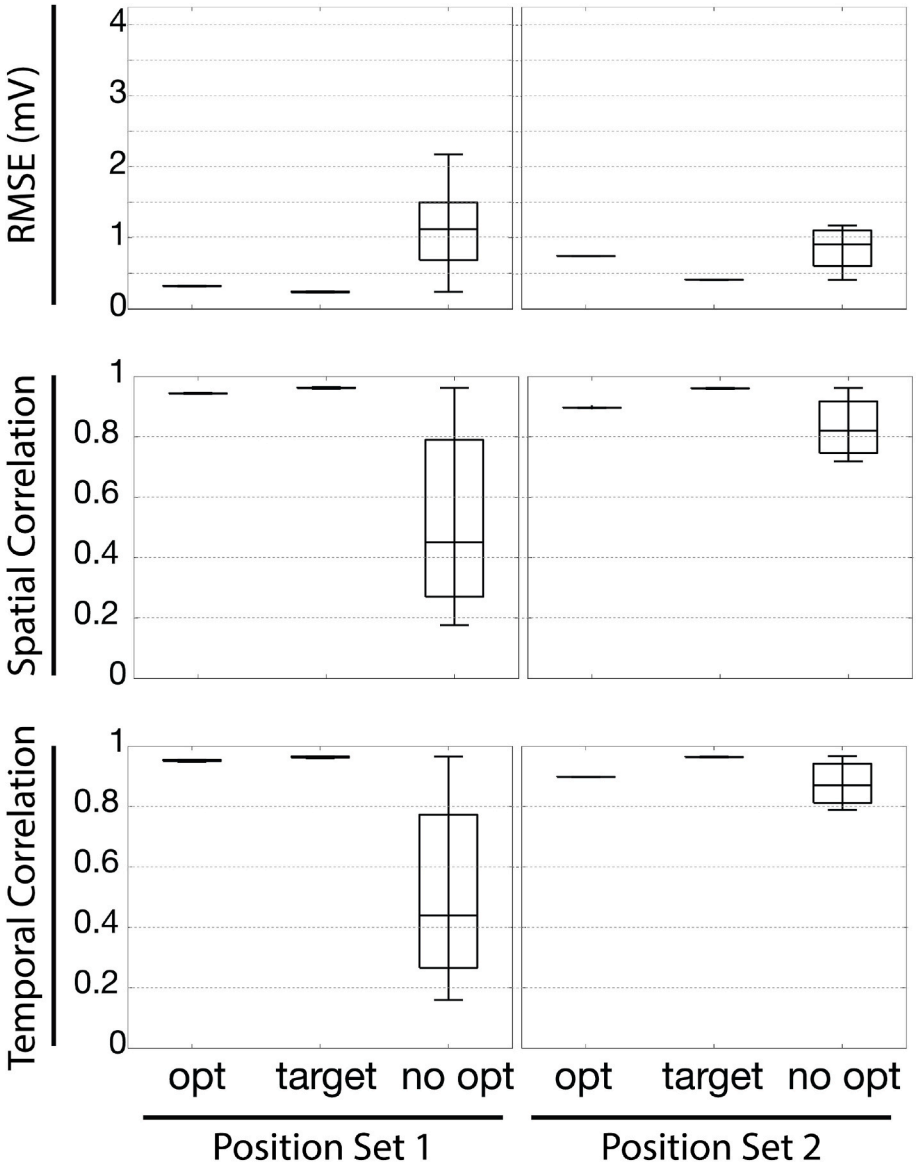

Fig. 8. ECGI accuracy as measured by RMSE, spatial correlation, and temporal correlation for Position Set 1 and 2 using the aVp activation sequence. Results are shown for the optimized cardiac positions (opt), true cardiac positions (target), and non-optimized positions (no opt). From top to bottom these statistics report the RMSE, spatial correlation (SC), and temporal correlation (TC). Within each row there are two panels. The ones on the left depicts the results for Position Set 1, and the ones on the right depicts the results for Position Set 2.

Table 5
Cardiac localization error and ECGI accuracy for Position Set 4, aVP activation sequence, using the small cardiac geometry. Averages and standard deviations were taken over all 100 positions. Mean per-electrode localization error (Loc. Err.) is in millimeters and root-mean-squared error (RMSE) is in millivolts. Spatial correlation (SC) and temporal correlation (TC) are scaled between −1 and 1. Values are shown as means ± one standard deviation.

Stat	Value
Loc. Err	6.50 ± 0.03 mm
RMSE	0.36 ± 0.00 mV
SC	0.93 ± 0.00
TC	0.94 ± 0.00

Supplemental Fig. 2, however the variability remained low for Position Set 4.

The potential map reconstructions in Fig. 9 illustrate that optimization resulted in consistent ECGI solutions, with only minor differences between best and worst case scenarios, and were more similar to the solutions found using the target positions than those using non-optimized positions. The same was true across all position sets.

Activation Sequences: We observed improvement in the ECGI reconstructions using optimized cardiac geometries over non-optimized geometries across all activation sequences, as shown in Table 7 and Supplemental Fig. 2. The aVp and the aVp1-40 activation sequences showed the highest ECGI accuracy as measured by SC and TC, while the sinus beat showed the lowest RMSE. However, the maximum root mean squared voltages from each of the activation sequences were 3.2 mV (aVP), 1.5 mV (sinus), and 3.6 mV (aVP1:40). Therefore the lower RMSE of the sinus beat does not necessarily indicate superior performance since the overall amplitude of the sinus case was lower as well.

LeadSets: We present the three metrics of ECGI reconstruction in Fig. 10 which includes (RMSE (top), SC (middle), and TC (bottom)) for solutions found with geometries that were optimized using each of the leadsets. Results using both the target and non-optimized cardiac geometries are also presented for comparison. We observed improvements in ECGI solutions using cardiac positions optimized with all leadsets, even in cases of severely reduced sampling coverage. As shown in the figure, optimization of the cardiac geometry using even the orthogonal leadset, which has the fewest (six) leads, improved ECGI accuracy. These improvements were more pronounced in the leadsets with increased

Table 6
Percentage of improvement of optimized geometries over non-optimized geometries according to all evaluation metrics. Each column shows a different testing scenario (position set and activation sequence). Each row shows the improvement (percent of heartbeats or geometries which show an improvement over the non optimized case) according to each metric: spatial correlation (SC), temporal correlation (TC), root mean squared error (RMSE), and per-electrode localization error (Loc. Err.).

	Set 1	Set 2	Set 1	Set 2	Set 1	Set 2	Set 3	Set 4
	aVP	aVP	Sinus	Sinus	aVP1:40	aVP1:40	aVP	aVP
SC	90%	68%	90%	44%	90%	65%	86%	90%
TC	93%	60%	100%	68%	90%	57%	89%	93%
RMSE	90%	64%	90%	64%	90%	60%	86%	90%
Loc. Err.	90%	64%	90%	68%	90%	65%	86%	90%

Table 7
ECGI accuracy across each Position Set and activation sequence for the full leadset. Root Mean Squared Error (RMSE) is in millivolts. Spatial correlation (SC) and temporal correlation (TC) are both standard correlation coefficients, scaled between −1 and 1. Values are shown as mean ± one standard deviation.

		Position Set 1	Position Set 2
RMSE (mV)	aVp	0.32 ± 0.00	0.44 ± 0.00
	sinus	0.18 ± 0.01	0.21 ± 0.01
	aVP1:40	0.35 ± 0.02	0.46 ± 0.03
SC	aVp	0.94 ± 0.00	0.90 ± 0.00
	sinus	0.83 ± 0.02	0.80 ± 0.02
	aVP1:40	0.93 ± 0.03	0.87 ± 0.07
TC	aVp	0.95 ± 0.00	0.90 ± 0.00
	sinus	0.93 ± 0.01	0.85 ± 0.01
	aVP1:40	0.91 ± 0.03	0.88 ± 0.04

sampling, for example all of the 3-strip leadsets, although we noted a decrease in accuracy for the 3-strip v2 leadset as compared to all the other 3-strip variations.

3.3. Improvements in variability of ECGI reconstructions

One of the most consistent observations from all testing scenarios was that geometric optimization reduced variability of the solutions compared to the non-optimized cases in all scenarios. This reduction in variability came in a few forms. With respect to geometric error, optimization reduced the variability in per-node localization error compared to unoptimized geometries, which appear as thinner box plots in Figs. 5 and 6 and Supplemental Fig. 2, as well as small standard deviations in Tables 3 and 4 With respect to ECGI accuracy, the ECGI solutions found using optimized geometries had reduced variability in RMSE, SC, TC, and the reconstructed potential maps compared to solutions found using non-optimized geometries, seen in thinner box plots in Figs. 8–10, and Supplemental Fig. 2, as well as smaller standard deviations in Tables 7 and 4

4. Discussion

In this study we established and validated a framework to estimate the position of the heart within the torso on a beat-by-beat basis using only noninvasively measured body-surface potentials. We validated the framework using a combination of three different sets of initial heart positions, three different sets of activation sequences, and thirteen different sets of body-surface recording electrodes. We examined both the accuracy of the position estimates and the effect of these geometric optimizations on ECGI reconstructions when compared to both the target and nonoptimized heart positions. We observed both a decrease in geometric error and an increase in ECGI accuracy using our geometric correction framework.

4.1. Reduction of variability

One of the most notable results from our study was the reduction of variability in both cardiac localization error and ECGI accuracy across all scenarios. Lower variability in ECGI solution accuracy could translate to enhanced clinical utility, as clinicians can have more confidence in any specific inverse solution if the variability associated with it is smaller.

For Position Sets 1, 3 and 4, which utilized an exaggerated range of motion, optimization resulted in reduced cardiac position error and improved ECGI accuracy for the vast majority of heart beats compared to the nonoptimized solutions, as seen in Table 6. There were, however, some cases in which the non-optimized position happened to coincide closely or exactly with the ground truth position and thus produced superior estimates compared to the optimized positions. This occurred because the optimization acts jointly on an entire collection of heartbeats and cardiac positions. Therefore errors incorporated into the optimization framework can be reflected in inaccurate absolute position estimates. However, these inaccuracies can been seen as a trade-off for the improved consistency in both cardiac geometry position and ECGI solution accuracy.

Position Set 2 showed reduced variability in geometric error and ECGI accuracy after optimization, while the mean error and mean accuracy were close to the mean error and accuracy of the non-optimized positions, in terms of both geometric reconstruction and ECGI solutions. Thus there were cases in Position Set 2 where the heart position was incorrectly moved farther from its true position, and the absolute ECGI accuracy suffered as a result (Table 6). However, the average heart position error and ECGI inaccuracy were roughly the same, if not a little lower, after optimization when compared to non optimized cases. Additionally, the variability in all metrics was reduced after optimization (Supplemental Fig. 2). Thus, even in Position Set 2, the optimization provided more reliable position estimates and ECGI solutions. We address the limitation of inaccurately moving the cardiac geometry from its target location further in Section 4.5.

4.2. Effects of different position sets

We explored the differences in geometric reconstruction and ECGI accuracy using three different Sets of cardiac positions. Position Set 1 encompassed a large range of possible uncertainty in heart position in order to examine the effects of a wide range of sources, *e.g.,* respiration, body position, image quality, or geometric model construction. Position Set 2 encompassed uncertainty over a much smaller range and was based on observed cardiac motion during an cine MRI acquisition. Position Set 3 consisted of 100 realizations of 100 random samples from the position range defined for Position Set 1. Since the optimization operates on a particular collection of heartbeats which have a particular set of target positions, we were concerned that the results would be affected by particular target positions. Position Set 3 was meant to address this concern by randomly sampling target positions of the cardiac geometry.

Overall, we found that cardiac position was reconstructed best in Position Sets 1, 3 and 4, with Set 4 having the lowest average localization error. We speculate that the improved results of Sets 1, 3, and 4 over Set 2 are caused by Set 2's decreased ranges of motion. We observed with Position Set 2 that the reconstructed geometries showed a high precision, but an accuracy that was off by what appeared to be a

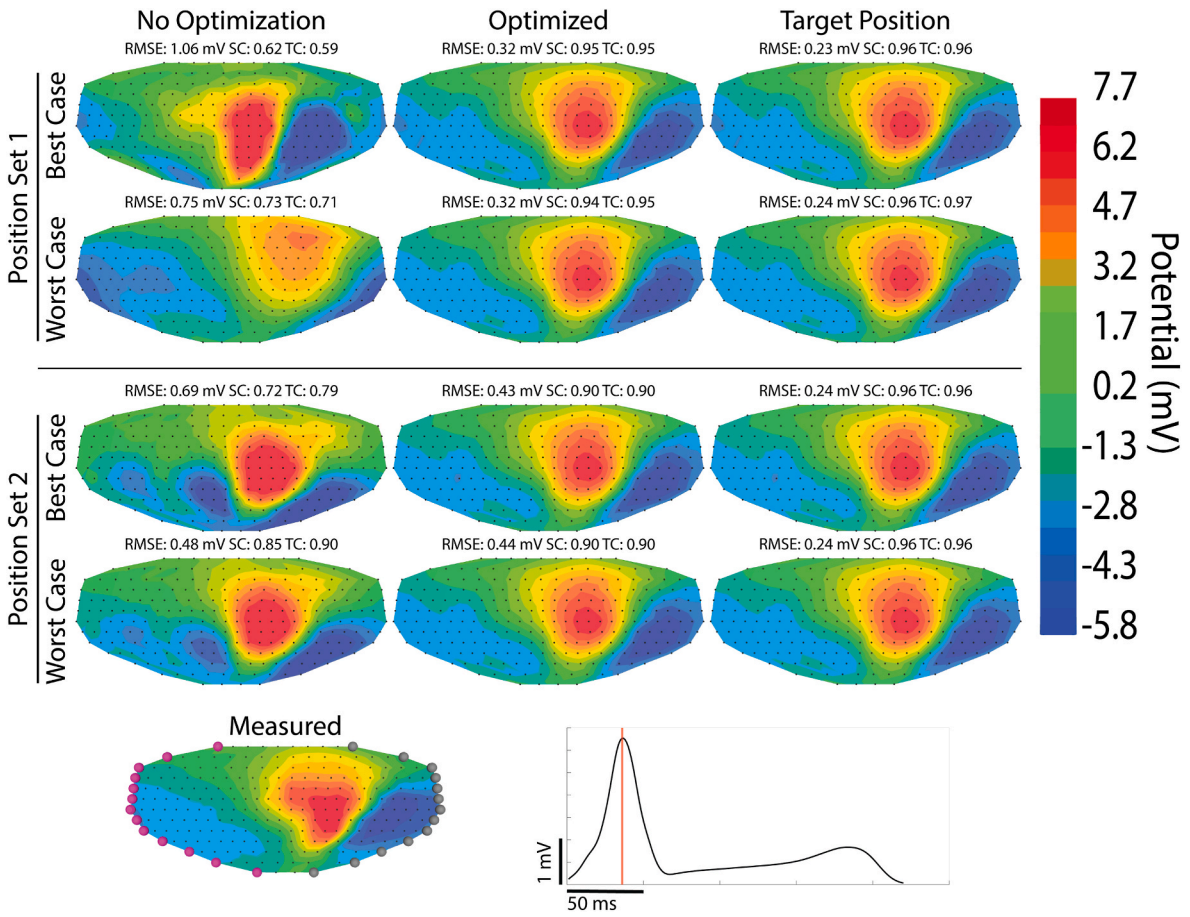

Fig. 9. Example ECGI reconstructions for the non-optimized, optimized, and ground-truth cardiac positions using Position Sets 1 and 2 with the aVp activation sequence. Best and worst case beats were determined based on the maximum and minimum spatial correlation of the optimized reconstruction compared to the true EGMs (shown on lower left) and were chosen separately per position set. All maps show potentials at a time corresponding to the peak of the RMS signal for the true EGMs, as indicated on the waveform plot on the lower right. The potential maps are displayed on a flattened and unwrapped geometry of the pericardiac cage. The colored nodes on the map of the measured potentials correspond to the vertical lines along which the cage was cut to produced the flattened projection. Video s.1 shows the cage geometry being unwrapped into this flattened version.

constant offset. We speculate that this is due to the existence of a null space in the optimization problem, in other words that there may be multiple sets of relative positions of the cardiac geometry that fit within the torso and satisfy our optimization equation. With Position Sets 1, 3 and 4, the algorithm may be less sensitive to the presence of this null space because the larger range of target positions of the heart, which may reduce the number of sets of positions that fall within the null space. We can see that even with Position Set 2, the z axis position, which has the largest range of all the parameters, was well reconstructed in both absolute and relative terms. The absolute reconstruction of Z in Position Set 2 is consistent with the idea that larger parameter ranges in the optimization can allow for better absolute position reconstruction. We discuss further consequences of this behavior in section 4.5 below. We also observed a more robust precision in Position Set 1 than Position Set 2 (Fig. 5). We suspect this result is due to larger differences in the BSP maps from heart positions from Position Sets 1, 3 and 4, a direct result of the larger range of motion. The optimization leverages the relative differences in BSP maps to identify relative differences in cardiac positions. Thus the larger differences in Position Sets 1, 3 and 4 may allow for more precise parameter reconstruction.

Across all Position Sets we observed that rotation parameters, and in particular yaw and roll, were more difficult to reconstruct accurately, especially when the angles were close to zero (See Fig. 5, and Supplemental Fig. 1). However, we did not observe a similar pattern in the reconstruction of translation parameters, nor did we note an increase in geometric error for the heartbeats for which these angles were small. We speculate that this loss in reconstruction accuracy for yaw and roll is due to another null space, or lack of uniqueness, due to an ambiguity between those two rotations. In particular we observed this poor reconstruction of yaw and roll when the third angle, pitch, was close to zero. In that case, geometrically, small changes in either yaw or roll result in similar, often very similar, changes in the position of the heart. Thus overall we believe that our parameterization may not be full identifiable; there are multiple combinations of the six parameters that can achieve the same or similar cardiac positions. This suggestion is consistent with our observation that despite these errors in parameter values, we observed very little variability in the error between reconstructed and target cardiac *geometries* across all Position Sets (see Supplemental Fig. 2 and Section 4.1).

ECGI accuracy was on average improved by geometric optimization, and the variability of the accuracy was reduced in all cases. In Position Set 1 there was a notable increase in ECGI accuracy after geometric optimization; indeed our results approached the accuracy seen using ground truth cardiac positions. Position Set 2 showed more modest ECGI improvement, but the variability in ECGI solution accuracy was reduced (Supplemental Fig. 2). The ECGI accuracy for optimized positions from Position Set 2 was often close to the mean ECGI accuracy seen with the non-optimized positions, which we attribute to the difficulty in resolving absolute position and the smaller differences in BSP maps in Position Set 2. In Position Set 2 our geometric correction framework did improve relative changes in position, and thus was able to produce ECGI solutions that had a low variability, but not necessarily substantially

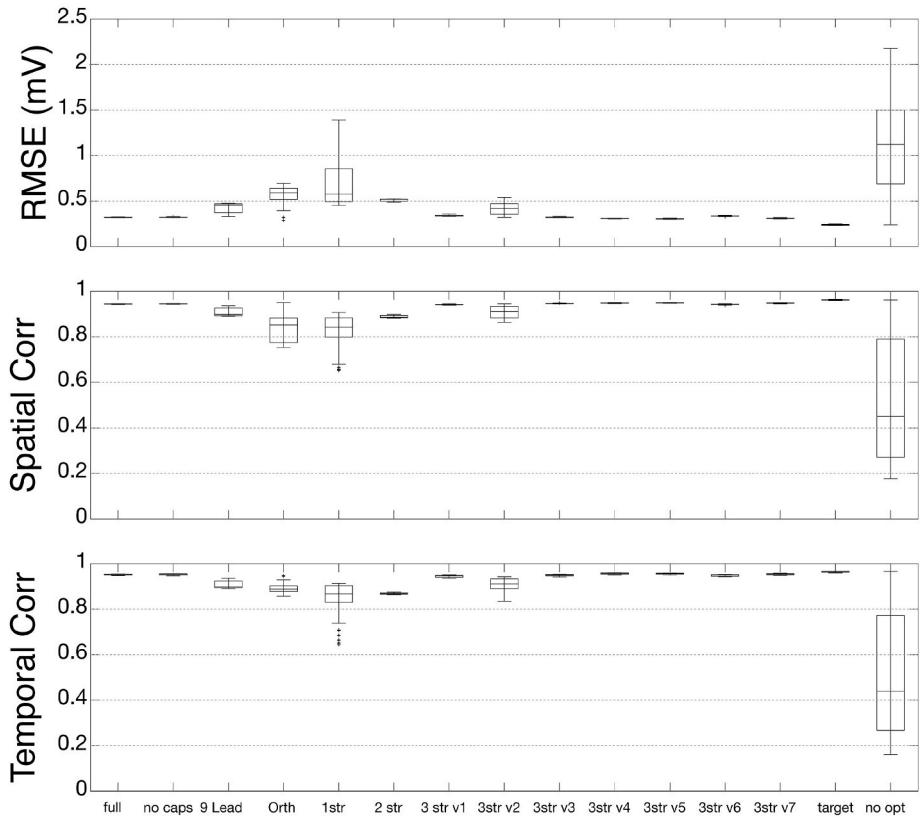

Fig. 10. ECGI reconstruction accuracy across the different leadsets using Position Set 1 and the aVp activation sequence. LeadSet names correspond to the those shown in Fig. 4.

improved accuracy. The relative position reconstruction is corroborated by the parameter reconstructions obtained for Position Set 2 (Fig. 5) which show a bias in the estimated parameters, generally following the trends of the relative true positions but not the absolute positions. We suggest that incorporation of constraints on the cardiac motion could help to reduce this ambiguity and result in further improvement in the geometric reconstruction and ECGI solutions. Furthermore, given the apparently stable nature of this offset, we suspect that if a single true cardiac position were known, it could be used to identify and remove the offset from all positions.

Beyond the inverse solution accuracy metrics, we also observed differences in the reconstructed potential maps using target, optimized, and non-optimized cardiac positions. Interpretation of potential maps in both research and clinical settings is primarily driven by observation of features on the maps such as the visually prominent patterns in Fig. 9. These features are often poorly captured by statistical metrics [29]. For example in Fig. 9 there are erroneous potential minima in the inverse reconstructions for the non-optimized positions that are either reduced or absent in solutions with the optimized positions. Furthermore, the shapes of the isocontours in the potential maps generated using the optimized positions appear to more closely match those of the measured potential maps than the potential maps generated from the non-optimized positions. We also observe these feature based difference using the sinus activation sequence (see Supplemental Fig. 4).

Position Set 3 showed comparable geometric and ECGI accuracy to Position Set 1 with a slightly higher degree of variability (Tables 3 and 7). This similarity between the performance of Position Sets 1 and 3 indicates that our geometric correction framework is relatively robust to the distribution of ground truth positions, although the slightly higher variability in both ECGI accuracy and geometric reconstruction does suggest minor sensitivity to the specific set of heartbeats and underlying target geometries to which the algorithm is applied.

In Position Set 4 we expected geometric optimization would be more difficult than in Position Set 1, as a smaller cardiac geometry might result in increased ill-conditioning in the ECGI inverse solutions, hence introducing errors to the geometric reconstruction. As expected, the experiments resulted in a slight degradation of the inverse solutions for results using both the ground truth cardiac positions and those after geometric correction with he smaller geometry (Supplemental Fig. 2). However, this increase in error did not translate into the geometric reconstruction, which improved for most heart beats in Position Set 4 (Table 6).The resulting localization error, measured by mean euclidean distance between target and reconstructed electrode positions, was smaller for Position Set 4 (6.50 $\pm$ 0.003 mm) than Position Set 1 (7.8 $\pm$ 0.09 mm, aVP activation sequence, full leadset). Moreover, when comparing the parameter reconstruction for Position Set 1, shown in Fig. 5, and parameter reconstruction for Position Set 4, shown in Supplemental Fig. 5, the reconstruction accuracy was strikingly similar. The correlation of individual parameter reconstructions (rows of the **P** matrix) between Position Sets 1 and 4 were high (0.99, 0.99, 0.99, 1.0, 1.0, 1.0, for pitch, yaw, roll, X, Y, Z parameters respectively). Only the rotation parameters showed some difference between the small heart geometry and the larger one.

4.3. Activation sequences

Geometric reconstruction and ECGI accuracy varied across activation sequences. We found that geometric reconstruction was slightly more accurate for the sinus beat for both Position Sets 1 and 2. On the other hand, results for the aVp1-40 activation sequence were the least accurate. This result might be expected given the natural beat-to-beat variability of the EGMs present in the aVp1:40 recordings, which is ignored in the algorithm. The smaller number of beats in aVp1:40, compared to the 100 heart beats for the sinus beat data sets, also may have contributed to this result. However, the increase in per node localization error for the aVP1:40 activation sequence compared to the

aVP activation sequence was small, within 1–2 mm of the aVp activation sequence.

ECGI accuracy was generally higher in the aVp and aVp1:40 activation sequences than the sinus activation sequence (Table 7). ECGI reconstructions of sinus rhythms are generally less accurate due to the increased complexity of such beats compared to ventricular paced rhythms and the lower signal amplitudes (RMS voltages of 1.5 mV for the sinus beat compared to 3.6 mV for the aVP1-40) [24]. This trend was observed across all position sets (Supplemental Fig. 2). Notably, however, geometric optimization in all cases resulted in reduced ECGI solution variability in each of the activation sequences.

4.4. Limited lead sets

We also examined the effect of limited torso surface sampling on cardiac position reconstruction error and resulting ECGI accuracy. We found that substantial improvements in geometric error could be achieved with even limited torso surface recordings, even as few as a single strip of electrodes (Fig. 4, Supplemental Fig. 3). While the leadsets that sampled more densely than the others (full, no caps, 3-strips v1) usually resulted in superior geometric reconstructions, there were some unanticipated results. The 3-strips v7 set, which is the most under-sampled version of the 3-strips leadset, produced cardiac positions that were on average more accurate than the 3-strips v2, which had more leads. In fact, the 3-strips v2 leadset produced inferior results as compared to all of the other 3-strip variations. We suspect that the difference in number of electrodes between 3-strips v2 and the other lead Sets (v2: 53 electrodes, v7: 16 electrodes for example) plays a less important role than the information content specific to the electrodes of the v7 Set. In other words, lead placement seemed to be more important in many cases than number of leads, as seen for example by comparing the 9-lead leadset with the 1-strip leadset (34 leads). In this case, the 9-lead leadset outperformed the geometric reconstruction with the 1-strip leadset, which we attribute to the better spatial coverage of the 9-lead leadset. We observed that cases with higher geometric reconstruction error than with the full leadset, such as the orthogonal and 1-strip sets, inaccurately reconstructed the X and Z parameters in particular (Supplemental Fig. 3).

ECGI accuracy was also improved by optimization in all leadsets, with similar trends in performance as for the geometric error (Fig. 10). In all cases, the geometric optimization also minimized ECGI variability substantially, even when very few leads were used for geometric optimization. We observed improvements in ECGI solution accuracy and variability that were comparable to using the full 771 leadset with as few as 16 leads (3-strips v7). These reduced leadsets allow for reduced computational complexity during geometric optimization while still providing robust cardiac position estimation.

4.5. Limitations

The main limitation of the geometric optimization framework described here is its inability to resolve consistently the absolute cardiac position. As can be seen in the results for Position Set 2, relative positions are accurately reconstructed, but absolute position can be more difficult to discern. This features is thought to be a result of a null space that exists in the associated optimization problem due to the fact that the method relies on relative differences in the BSP maps to resolve cardiac position. Position Set 1 avoids this problem by having a larger range of motion, thereby restricting the space of possible sets of relative positions available to the optimization. A future improvement to this method would be to implement regularization operations to enforce assumptions such as known cardiac positions or other information. Such known positions could be derived from either static imaging (such as a CT or MRI) or more coarse but more easily applied imaging modalities such as ultrasound, which could provide approximate known cardiac positions associated with specific BSP map recordings. The optimization space could also be reduced when a low range of motion is suspected. Even without addressing this limitation, our geometric optimization framework was still able to reduce the variability in ECGI solution accuracy that is linked to ambiguity in heart position.

A further limitation of the study was the use of simulated datasets for validation. While simulations rarely capture the true variability that arises in the biological application, they do offer highly controlled conditions in a setting where absolute ground-truth heart position is known and to which known variations could be applied. This framework allowed us to robustly examine the performance of the geometric correction framework under a wide variety of conditions. Naturally, future studies will be needed to validate this approach on experimental and eventually clinical data. Our simulations were also based on a single torso geometry that did not contain internal organs, both of which provide additional types of modeling uncertainty. Our goal, however, was to focus on a challenging and known source of error—the position of the heart within the torso. The type of motion we modeled was also along a small set of positions within the torso geometry. The heart moves with respiration, with contraction, and with body position, which may encompass more positions than we tested here. However we have demonstrated that the optimization method we propose can compensate for errors associated with cardiac motion. Moreover, the approach we describe has substantial flexibility and could be adapted to other sources and types of geometric error. We also limited the evaluation to a single set of electrograms as the cardiac source to be reconstructed for most of the study. We assume that the cardiac source is the same between heartbeats, however beat to beat variability is a relevant physiological concern. To address this limitation, we created the aVp1:40 activation sequence set, with promising results. However, a more robust examination of the effects of beat to beat variability on our method is a natural future step. Furthermore, inclusion of multiple activation sequences types simultaneously is a clinically useful target for improvement of our algorithm.

The use of simulated datasets also introduces another limitation, in that the same forward solver was used in both the generation of the BSP signals and the inverse formulation. This is regarded as an ‘inverse crime’ as synthetic data generated in this way is free of many of the common sources of error and can lead to overconfidence in the resulting inverse solutions. To mitigate this overconfidence, we have added white noise to the generated BSP signals, a practice that conforms to standards in the field [30–33]. In this study it was necessary to have the full control of synthetic BSP data in order to thoroughly validate the performance of our algorithm in a scenario in which true cardiac position and EGM were known. Other options, e.g., generating the synthetic BSPM with alternative numerical solutions or adding small errors in the torso/heart geometries to introduce further error, are each fraught with their own weaknesses as it is unclear how much of such errors to add in order to replicate real world conditions.Future studies will be needed to address this limitation, e.g., using experiments in which the heart position is moved in a controlled manner concurrently with BSP and EGM recordings. Despite the limitation introduced using synthetic BSP data, the datasets presented in this study allowed for control over aspects (e.g., ranges of motion, number of positions, accuracy of true cardiac position, and control of cardiac source potentials) that would be impractical in an experimental setup.

A further limitation of all studies that make use of BSP mapping is the inconsistent application of leadsets. The range of numbers of electrodes described in the literature is broad, *e.g.,* 32–300, as is the placement relative to anatomical landmarks [34]. In consequence, the success of any approach based on BSP mapping could be expected to depend on the specific leadset. To address this source of variability, we included a range of limited-lead sampling in the present study and achieved acceptable results even with greatly reduced numbers of leads.

4.6. Prospective view

The motivation for optimizing to account for variable (or incompletely known) heart position was the observation that this is a common source of error in the forward model that is the basis for ECGI. However, generalizations to include the other organs such as the lungs would be straightforward as long as the appropriate position constraints were applied to avoid surface crossings. Furthermore, addressing other modeling errors would only require including parametrerizations of the modeling errors in the input set and applying them during the forward model generation. Such modeling errors and areas of uncertainty include organ conductivity, electrode placement, torso shape, among others [35–38]. Examination of the effects of these errors and uncertainties has been explored in a number of other studies. Application of our optimization framework could allow for resolution of some of these areas of uncertainty and aid in the creation of patient specific digital-twin models. Increases in complexity may require additional constraints, but the flexibility of our optimization framework to allow for reconstruction of other variables of interest presents a powerful tool for improving ECGI.

We note that our geometric reconstruction method provides a way to improve contemporary ECGI implementations with minimal changes or additional costs to the clinical workflow, as BSP recordings lasting for multiple consecutive beats can be readily obtained. These multiple recordings can then be used to optimize the geometric model and improve solution accuracy and reliability as we have shown in this study. Such continuous recordings in combination with our geometric correction methods could then be fed into further advanced methods for improving the ECGI solution, such as applying the joint inverse method to achieve a single inverse solution which takes into account all of the positional variation [19].

A possible application of this geometric optimization framework would be in the creation of an 'imageless' ECGI system, that would not rely on MRI or CT scans for the cardiac geometric model. Instead, such a method would utilize either a generic geometric model or one based on some previous imaging study. Our geometric correction framework could then optimize the placement of the heart inside the torso without the need for costly imaging modalities such as MRI. Without the need for advanced medical imaging and subject-specific segmentation to construct the torso and cardiac geometries, the barrier to use ECGI would be greatly reduced. Such a method would still require addressing the limitation of the null space present in the method proposed in this study. As a compromise, less complicated and costly imaging modalities such as ultrasound could provide enough information to constrain the geometric reconstruction and reduce ambiguity in the heart position. We also note in our study that we achieved geometric reconstruction and improved ECGI accuracy on par with using the maximum sampling leadset (the full leadset) with many of the reduced sampling leadsets, including the 9 lead leadset. Such limited leadsets allow for a lighter computational burden in addition to being more feasible in many clinical scenarios.

Our implementation of this geometric optimization framework leveraged the matlab parallel processing toolbox and was executed using high end computational resources. However, the optimization was far from real time, with most cases taking upwards of an hour to complete. We anticipate that the computational efficiency of the current implementation could certainly be improved. An implementation in languages such as C++ or python could allow for leveraging of GPU based computations, which we anticipate could result in substantial speedup. Further development of this optimization framework to reduce computation time could further improve its eventual clinical utility.

5. Conclusions

In this study we have presented and validated a framework to correct geometric error in the torso model for use in ECGI. Specifically we have targeted a common source of error in ECGI, errors in localization of the heart within the torso. We have shown that our geometric correction framework is able to reconstruct the cardiac position using only body surface potential recordings in a set of in-silico experiments based on actual canine experimental recordings. We also examined the effect of geometric correction on ECGI solutions, and showed that our geometric correction framework resulted in reconstructions with increased accuracy and reduced variability.

We explored the use of our optimization framework to correct for geometric errors, specifically cardiac mislocalization. Generalizations to other sources of error in ECGI would be straight forward. For example, other parameters of the forward model such as conductivity and position of other organs of interest could be optimized in a similar manner. We even speculate that this framework could open the door for imageless ECGI methodologies and even estimate the shape of the heart to some degree using a shape model parameterization of the heart such as the one described in Tate et al. [39]. The optimization framework presented here provides a unique opportunity to address a variety of sources of error common in ECGI implementations, by leveraging fully noninvasive measurement techniques.

Industry relationships

Dr. Wilson W. Good has recently joined Acutus Medical. None of the research described or performed for this study was influenced by this relationship and there is no potential conflict.

Acknowledgment

This research was supported by NIH NHLBI grant no. F30HL149327 (J.A.B, L.C.R., R.S.M.); NIH NIGMS Center for Integrative Biomedical Computing (www.sci.utah.edu/cibc), NIH NIGMS grants P41GM103545 and R24 GM136986 (J.A.B, L.C.R., R.S.M.); the NSF GRFP (L.C.R); the Utah Graduate Research Fellowship (J.A.B); and the Nora Eccles Treadwell Foundation for Cardiovascular Research (J.A.B, L.C.R., R.S.M.)

Appendix A. Supplementary data

Supplementary data to this article can be found online at https://doi.org/10.1016/j.compbiomed.2021.105174.

References

[1] M. Cluitmans, D. Brooks, R. MacLeod, O. Dossel, M. Guillem, P. van Dam, J. Svehlikova, B. He, J. Sapp, L. Wang, L. Bear, Validation and opportunities of electrocardiographic imaging: from technical achievements to clinical applications, Front. Physiol. 9 (2018) 1305.

[2] E. Wissner, A. Revishvili, A. Metzner, A. Tsyganov, V. Kalinin, C. Lemes, A. M. Saguner, T. Maurer, S. Deiss, O. Sopov, E. Labarkava, M. Chmelevsky, K. H. Kuck, Noninvasive epicardial and endocardial mapping of premature ventricular contractions, Europace 19 (2017) 843–849.

[3] D. Erkapic, T. Neumann, Ablation of premature ventricular complexes exclusively guided by three-dimensional noninvasive mapping, Card Electrophysiol Clin 7 (2015) 109–115.

[4] D. Potyagaylo, M. Segel, W.H.W. Schulze, O. Dössel, Noninvasive localization of ectopic Foci: a new optimization approach for simultaneous reconstruction of transmembrane voltages and epicardial potentials BT, in: S. Ourselin, D. Rueckert, N. Smith (Eds.), Functional Imaging and Modeling of the Heart, Springer Berlin Heidelberg, Berlin, Heidelberg, 2013, pp. 166–173.

[5] P. Cuculich, C. Robinson, Noninvasive ablation of ventricular tachycardia, N. Engl. J. Med. 378 (2018) 1651–1652.

[6] Y.S. Dogrusoz, L.R. Bear, J. Bergquist, R. Dubois, W. Good, R.S. MacLeod, A. Rababah, J. Stoks, Effects of interpolation on the inverse problem of electrocardiography, in: 2019 Computing in Cardiology (CinC), 2019, https://doi.org/10.23919/CinC49843.2019.9005869, 1–Page 4.

[7] S. Schuler, M. Schaufelberger, L.R. Bear, J.A. Bergquist, M.J.M. Cluitmans, J. Coll-Font, Önder N. Onak, B. Zenger, A. Loewe, R.S. MacLeod, D.H. Brooks, O. Dössel, Reducing line-of-block artifacts in cardiac activation maps estimated using ecg imaging: a comparison of source models and estimation methods, Trans. Biomed. Eng. (2021), https://doi.org/10.1109/TBME.2021.3135154.

[8] L. Bear, J. Svehlikova, J. Bergquist, W. Good, A. Rababah, J. Coll-Font, R. MacLeod, E. van Dam, R. Dubois, Impact of baseline drift removal on ecg beat classification and alignment, in: 2021 Computing in Cardiology, Press, 2021, pp. 1–4.
[9] J.A. Bergquist, J. Coll-Font, B. Zenger, L.C. Rupp, W.W. Good, D.H. Brooks, R. S. MacLeod, Improving localization of cardiac geometry using ecgi, in: 2020 Computing in Cardiology, 2020, pp. 1–4, https://doi.org/10.22489/CinC.2020.273.
[10] J.A. Bergquist, B. Zenger, W.W. Good, L.C. Rupp, L.R. Bear, R.S. MacLeod, Novel experimental preparation to assess electrocardiographic imaging reconstruction techniques, in: 2020 Computing in Cardiology, 2020, pp. 1–4, https://doi.org/10.22489/CinC.2020.458.
[11] J. Svehlikova, J. Lenkova, A. Drkosova, M. Foltin, M. Tysler, Ecg based assessment of the heart position in standard torso model, in: Á. Jobbágy (Ed.), 5th European Conference of the International Federation for Medical and Biological Engineering, Springer Berlin Heidelberg, Berlin, Heidelberg, 2012, pp. 474–477.
[12] J. Coll-Font, D.H. Brooks, Tracking the position of the heart from body surface potential maps and electrograms, Front. Physiol. 9 (2018) 1727.
[13] M. Rodrigo, A.M. Climent, A. Liberos, I. Hernandez-Romero, A. Arenal, J. Bermejo, F. Fernandez-Aviles, F. Atienza, M.S. Guillem, Solving inaccuracies in anatomical models for electrocardiographic inverse problem resolution by maximizing reconstruction quality, IEEE Trans. Med. Imag. 37 (2018) 733–740.
[14] M. Milanic, V. Jazbinsek, R. Macleod, D. Brooks, R. Hren, Assessment of regularization techniques for electrocardiographic imaging, J. Electrocardiol. 47 (2014) 20–28.
[15] D. Swenson, S. Geneser, J. Stinstra, R. Kirby, R. MacLeod, Cardiac position sensitivity study in the electrocardiographic forward problem using stochastic collocation and BEM, Ann. Biomed. Eng. 30 (2011) 2900–2910.
[16] D. Sutherland, D. McPherson, C. Spencer, C. Armstrong, B. Horacek, T. Montague, Effects of posture and respiration on body surface electrocardiogram, Am. J. Cardiol. 52 (1983) 595–600.
[17] J.N. Amoore, Y. Rudy, J. Liebman, Respiration and the ecg: a study using body surface potential maps, J. Electrocardiol. 21 (1988) 263–271.
[18] M.G. Adams, B.J. Drew, Body position effects on the ecg: implication for ischemia monitoring, J. Electrocardiol. 30 (1997) 285–291.
[19] J.A. Bergquist, J. Coll-Font, B. Zenger, L.C. Rupp, W.W. Good, D.H. Brooks, R. S. MacLeod, Simultaneous multi-heartbeat ecgi solution with a time-varying forward model: a joint inverse formulation, in: D.B. Ennis, L.E. Perotti, V.Y. Wang (Eds.), Functional Imaging and Modeling of the Heart, Springer International Publishing, Cham, 2021, pp. 493–502, https://doi.org/10.1007/978-3-030-78710-3_47.
[20] V. Gisbert, S. Jiménez-Serrano, E. Roses-Albert, M. Rodrigo, Atrial location optimization by electrical measures for electrocardiographic imaging, Comput. Biol. Med. 127 (2020), 104031.
[21] M. Toloubidokhti, P.K. Gyawali, O.A. Gharbia, X. Jiang, J.C. Font, J.A. Bergquist, B. Zenger, W.W. Good, D.H. Brooks, R.S. MacLeod, L. Wang, Deep adaptive electrocardiographic imaging with generative forward model for error reduction, in: D.B. Ennis, L.E. Perotti, V.Y. Wang (Eds.), Functional Imaging and Modeling of the Heart, Springer International Publishing, Cham, 2021, pp. 471–481.
[22] K. Aras, Bioelectric Source Characterization of Acute Myocardial Ischemia, University of Utah, 2015. Ph.D. thesis.
[23] B. Burton, J. Tate, B. Erem, D. Swenson, D. Wang, D. Brooks, P. van Dam, R. MacLeod, A toolkit for forward/inverse problems in electrocardiography within the SCIRun problem solving environment, in: Proceedings of the IEEE Engineering in Medicine and Biology Society 33rd Annual International Conference, IEEE Eng. in Med. and Biol. Soc., 2011, pp. 1–4.
[24] J.A. Bergquist, W.W. Good, B. Zenger, J.D. Tate, L.C. Rupp, R.S. MacLeod, The electrocardiographic forward problem: a benchmark study, Comput. Biol. Med. 134 (2021), 104476.
[25] B. Zenger, J.A. Bergquist, W.W. Good, B. Steadman, R.S. MacLeod, High-capacity cardiac signal acquisition system for flexible, simultaneous, multidomain acquisition, in: 2020 Computing in Cardiology, 2020, pp. 1–4, https://doi.org/10.22489/CinC.2020.188.
[26] A. Rodenhauser, W. Good, B. Zenger, J. Tate, K. Aras, B. Burton, R. MacLeod, PFEIFER: preprocessing framework for electrograms intermittently fiducialized from experimental recordings, J. Open Source Software 3 (2018) 472.
[27] B. Messinger-Rapport, Y. Rudy, Regularization of the inverse problem in electrocardiography: a model study, Math. Biosci. 89 (1988) 79–118.
[28] R. MacLeod, R. Miller, M. Gardner, B. Horacek, Application of an electrocardiographic inverse solution to localize myocardial ischemia during percutaneous transluminal coronary angioplasty, J. Cardiovasc. Electrophysiol. 6 (1995) 2–18.
[29] L.R. Bear, L.K. Cheng, I.J. LeGrice, G.B. Sands, N.A. Lever, D.J. Paterson, B. H. Smaill, Forward problem of electrocardiography: is it solved? Circulation: Arrhythmia Electrophysiol. 8 (2015) 677–684.
[30] R. MacLeod, D. Brooks, Validation approaches for electrocardiographic inverse problems, in: P. Johnston (Ed.), Computational Inverse Problems in Electrocardiography, WIT Press, Ashurst, UK, 2001, pp. 229–268.
[31] Y. Serinagaoglu, D. Brooks, R. MacLeod, Improved performance of Bayesian solutions for inverse electrocardiography using multiple information sources, IEEE Trans. Biomed. Eng. 53 (2006) 2024–2034.
[32] A. Pullan, L.K. Cheng, M. Nash, D. Brooks, A. Ghodrati, R. MacLeod, The inverse problem of electrocardiography, in: P. Macfarlane, A. van Oosterom, O. Pahlm, P. Kligfield, M. Janse, J. Camm (Eds.), Comprehensive Electrocardiology, Springer Verlag, London, UK, 2010, pp. 299–344.
[33] M. Rodrigo, A. Climent, A. Liberos, I. Hernandez-Romero, A. Arenal, J. Bermejo, F. Fernandez-Aviles, F. Atienza, M. Guillem, Solving inaccuracies in anatomical models for electrocardiographic inverse problem resolution by maximizing reconstruction quality, IEEE Trans. Med. Imag. 37 (2018) 733–740.
[34] J. Bergquist, L. Rupp, B. Zenger, J. Brundage, A. Busatto, R. MacLeod, Body Surface Potential Mapping: Contemporary Applications and Future Perspectives 2, Hearts, 2021, pp. 514–542.
[35] D. Potyagaylo, O. Doessel, P. Van Dam, Influence of modeling errors on the initial estimate for nonlinear myocardial activation times imaging calculated with fastest route algorithm, IEEE (Inst. Electr. Electron. Eng.) Trans. Biomed. Eng. 9294 (2016), 1–1.
[36] L. Bear, R. Dubois, N. Zemzemi, Optimization of organ conductivity for the forward problem of electrocardiography, in: 2016 Computing in Cardiology Conference (CinC), 2016, pp. 385–388.
[37] A. Rahimi, L. Wang, Sensitivity of noninvasive cardiac electrophysiological imaging to variations in personalized anatomical modeling, IEEE (Inst. Electr. Electron. Eng.) Trans. Biomed. Eng. 62 (2015) 1563–1575.
[38] R.T. Jones, W.H.W. Schulze, D. Potyagaylo, O. Dössel, F.M. Weber, Computing lead-field matrices for a body tissue conductivity range, Biomed. Tech. 58 (2013), 000010151520134157.
[39] J.D. Tate, W.W. Good, N. Zemzemi, M. Boonstra, P. van Dam, D.H. Brooks, A. Narayan, R.S. MacLeod, Uncertainty quantification of the effects of segmentation variability in ecgi, in: D.B. Ennis, L.E. Perotti, V.Y. Wang (Eds.), Functional Imaging and Modeling of the Heart, Springer International Publishing, Cham, 2021, pp. 515–522.